Journal of Manufacturing Processes 131 (2024) 2118–2132

Contents lists available at ScienceDirect

Journal of Manufacturing Processes

journal homepage: www.elsevier.com/locate/manpro

Structure-performance relationships of multi-material jetting polymeric composites designed at the voxel scale: Distribution and composition effects

Niusha Daneshdoost *, Jacob Peloquin, Ken Gall

Department of Mechanical Engineering and Materials Science, Duke University, Durham, NC 27708, USA

ARTICLE INFO

Keywords:
Multi-material jetting
Voxel-scale design
Mechanical properties

ABSTRACT

Multi-material jetting (MMJ) allows for printed parts with intricate distributions of photopolymer materials deposited through hundreds of tiny nozzles at the voxel design scale. In this study, the mechanical tensile performance of various two-material composite designs is compared with respect to various volumetric ratios of two constituent materials, one rigid and strong and the other soft and ductile. Layered samples exhibited convergent, alternating layer failure due to interfacial bonding and fracture mechanisms of the dissimilar materials. To assist with predicting deformation profiles and explaining this behavior, a multilayer composite model was developed. Additionally, newly accessible voxel-scale digital material creation software was used to create custom "digital material" (DM) composites with a greater range of tunable strength, stiffness, and modulus of toughness over multilayer composites and manufacturer preset DM composites. Specifically, custom DMs increased the tunable ranges of ultimate strength and Young's modulus by 25.8 % and 5.5 %, respectively, and the achievable modulus of toughness by 56.3 % over the other composites. This study highlights the benefit of utilizing the full potential of MMJ by creating composite geometries designed at the voxel scale and provides groundwork for future comparative studies where customized voxel-scale material distributions can be tuned to achieve a desired mechanical performance over traditional composite designs.

1. Introduction

Over the past few decades, Additive Manufacturing (AM) or 3D printing has emerged as a revolutionary technology that has been selected over traditional manufacturing methods due to its unique advantages such as reduced material waste, customization for complex designs, and time and cost efficiency for low-volume production and rapid prototyping [1–4]. AM has been used in fields such as medicine, engineering, construction, fashion, and oceanography, and the applications continue to expand with increased research and development in the field [2–5]. AM is a process in which 3D parts are created using a combination of computer-aided design (CAD) software and a layer-by-layer manufacturing process [3,4]. This "additive" process allows for faster iterative prototyping, customizability for each part manufactured, and cost savings on molding and other tooling for low-volume production [3].

This layer-by-layer AM process has expanded the possibilities for creating multi-material composites with unique properties. These composites contain specific geometric distributions of two or more materials to achieve desired properties, appearance, or functionality. While not all AM methods are capable of multi-material printing, there are several methods that have seen advancement in multi-material printing capability, particularly for polymer materials, including fused filament fabrication (FFF), selective laser sintering (SLS), and digital light projection (DLP) [2,3,5–7].

With FFF, a thermoplastic polymer filament is softened and pushed through a nozzle that outlines and fills in the cross-sectional layers of the structure one layer at a time [5]. Typically, multi-material components can be achieved with FFF using multiple nozzles or switching feedstock at each layer; however, this is time consuming and can result in poor adhesion between materials. SLS printing involves distributing a thin layer of a powder-form thermoplastic material and selectively melting and re-solidifying specific cross-sectional layers using a targeted laser [7]. While precise control of multi-material powder distribution within layers proved challenging with this method, functionally graded and selectively deposited SLS composites have been achieved such as through the work of Levy et al. and Eckes et al., respectively [8,9]. Whereas FFF and SLS printing make use of meltable thermoplastic

* Corresponding author.
E-mail address: niusha.daneshdoost@duke.edu (N. Daneshdoost).

https://doi.org/10.1016/j.jmapro.2024.10.009
Received 30 May 2024; Received in revised form 26 September 2024; Accepted 7 October 2024
Available online 18 October 2024

materials, DLP performs a photopolymerization of monomer resin with targeted UV light to produce solidified thermosetting parts, which can be more suitable for applications requiring high thermal resistance. Traditionally, vats containing a single photopolymer resin material have been used for DLP printing. However, Ge et al. and Kowsari et al. were able to achieve multi-material composites using DLP and moveable glass plates containing puddles of different precursor solutions of photopolymer resin [10,11].

Although advancements have been made in the multi-material printing capabilities of FFF, SLS, and DLP technology, composites created using these methods face certain limitations. For example, DLP multi-material printing is restricted to creating layered composites as selectively combining two resin materials within a single layer remains challenging [10,11]. Furthermore, composites printed with FFF or SLS are tunable only at a relatively large scale based on the diameter of the extrusion nozzle in FFF printing or the shape and size distribution of particles in SLS printing [8,9,12].

In recent years, there have been marked improvements to another AM method, material jetting [13–19]. Material jetting (MJ), including multi-material jetting (MMJ), is a printing technology that uses a voxel-by-voxel material deposition method to allow for intricate composite structures of two or more materials within printed parts and a resolution as fine as 14 μm. As the print head moves over the bed, monomeric photopolymer resin is heated to reduce viscosity and dispensed at high speed through hundreds of tiny holes spread across eight cartridges on the printhead. The deposited droplets are then immediately polymerized using a UV curing light attached to the printhead. Once a single layer of material has been deposited across the build plate, the build plate moves downward and the printhead repeats the deposition and curing process. This novel printing method has expanded the capabilities of additive manufacturing in general by solving issues of post-curing requirements, enabling fabrication of previously unobtainable geometries, and distributing materials in voxel-scale patterns during printing [2,6,17,20–25]. No other printing technology currently has this ability, and it has offered a wide range of unique opportunities from increased range of material properties to complex geometric distributions of materials [2,6,14,22,26,27]. The most prevalent "versions" of MJ used in commercially available printing machines are Stratasys "PolyJet" technology and 3D Systems "MultiJet" technology.

MJ and MMJ studies to date have focused primarily on process parameter effects [12,16,28–36], creation of composites and metamaterials [14,22,25,26,32,37–41], and selection of materials for achieving certain tissue-like properties [19,27,39,42]. Fundamental work from researchers such as Aslani et al., Bass et al., Gay et al., Vu et al., Wei et al., and Yap et al. has created a foundational understanding of build plate orientation, location, spacing, and layer thickness effects on mechanical performance and part quality [30,33–36,43], thus providing valuable information on the limitations and capabilities of this printing method. This collection of work highlights anisotropy in printed components, with build orientation along the x-axis providing superior mechanical performance. Minimum attainable feature size and dimensional accuracy across length scales have also been investigated by these researchers along with Meisel et al., who showed that features less than 2 mm show statistically significant reduction in thermomechanical performance [30,32,36]. The effects of these process parameters on mechanical performance have been further studied, demonstrating significant effects from build plate orientation, post processing techniques, and surface finish ("Glossy" or "Matte") [12,29,34,35]. Unique to MJ and MMJ, fully enclosing support material has been shown to significantly impact surface quality and mechanical performance depending on methods of support removal and selection of surface finish [28,29,33,35,36,43].

Due to the voxel-scale material deposition capabilities of MMJ, researchers have turned to this printing technology for creating composites and functionally graded materials (FGM). Mesoscale composite designs were created by Yuan and co-authors to investigate the effects of relative voxel size on thermomechanical properties [23] and shape-memory behavior [44] of grid-like composites consisting of one rigid and one soft material. Similar work was performed by Ulu and co-authors, where the mechanical properties of grid-like and layered composites manufactured with MMJ were compared [24,25]. In a study conducted by Tee et al., mechanical strength, elasticity, and toughness were investigated for composites consisting of stiff ellipsoidal reinforcement particles suspended in a softer matrix [37]. Print orientation and topography of the suspended stiff particles were varied to understand their effect on the mechanical performance of the composites.

Many preset "digital materials" (DMs), which are combinations of existing materials available through manufacturer software packages, have been studied to understand the impacts of geometric distribution and volumetric ratio of constituent materials on multi-material composite mechanical properties. Meisel and co-authors investigated the relationship between viscoelastic properties of preset DMs based on their volumetric ratio of Stratasys VeroWhite+ and showed that the materials behave similarly to what can be predicted using the iso-strain boundary of the rule of mixtures [32]. Furthermore, the mechanical behavior of preset DMs consisting of Stratasys VeroWhite and TangoBlack materials were investigated by Bass et al. and Lumpe et al., who focused on material aging and interfacial relationships of the preset DMs, respectively [34,45].

As an extension of preset DMs, PolyJet technology offers a range of proprietary "digital anatomy" material combinations meant to mimic the stiffness of various human tissues [46]. Fig. 1 illustrates that MMJ, in this case PolyJet technology, provides an opportunity for fine tuning the mechanical properties of printed parts to achieve properties as strong and stiff as tendon or as soft and ductile as silicone rubber. Preset DMs composed of a soft elastomeric polymer and machine cleansing fluid were used by Bezek and co-authors to print multiple composites for various testing including dynamic mechanical analysis (DMA) and puncture testing, which ultimately demonstrated expanded capability of MMJ for creating tissue-mimicking printed materials [27]. In a study by Ionita et al., the potential for creation of patient specific vascular phantoms with 3D printing was investigated [47].

While the benefits of preset DMs and "digital anatomy" materials are well-documented, the voxel-scale material deposition capability of MMJ has motivated researchers to pursue customized multi-material composites with geometric distributions specified at the voxel scale. In a study conducted by Ituarte et al., they used MMJ to examine the effects of custom DM gradients on the mechanical properties of FGMs. Specimens were printed with either longitudinal grading, lateral grading, or biaxial grading and were tested monotonically in tension to determine if the combination of the two materials impacted the Young's modulus and which gradation had the largest effect [48]. Anatomically inspired custom DMs were implemented by Doubrovski et al. to map local tissue mechanical properties to various regions within fabricated sockets for prosthetic limbs [21]. Kaweesa et al. performed a fundamental analysis on the effects of design and process parameters for custom DM mechanical performance [22]. In this study, the size, shape, and distribution of rigid particles suspended in a soft polymer matrix were varied, and the resulting tensile modulus and tensile strength of composites were determined experimentally and modeled using rule of mixture (ROM) based equations.

Through these prior research efforts, MMJ has been established as a successful and practical method for producing multi-material composites. The voxel-scale design and material deposition made possible with MMJ enable creation of composites with a wide range of geometric distributions, from traditional layered designs to preset and custom

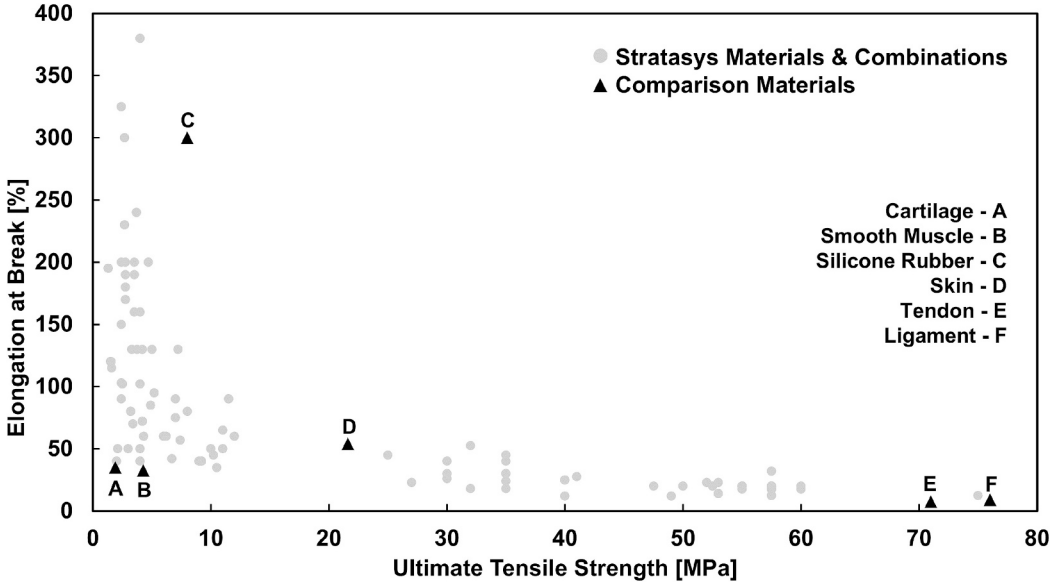

Fig. 1. This plot demonstrates the wide range of obtainable mechanical properties for parts created with MMJ and the Stratasys J750 Digital Anatomy Printer. The Stratasys materials are compared with silicone rubber, one of the most common elastomeric polymer materials, and with properties of various human tissues that are often mimicked in 3D printed biomaterials and medical devices.

Table 1
Mechanical property data for the Vero and Agilus resin families reported by Stratasys.

Material name	Young's modulus [MPa]	Ultimate strength [MPa]	Elongation at break [%]	Shore hardness
Vero (RM)	2200–3000	40–55	5–20	83D–86D
Agilus (SM)	Not listed	2.4–3.1	220–270	30A–35A

DMs. However, the relative mechanical performance among these different geometric distributions with respect to fixed volumetric ratios of constituent materials remains largely unstudied. Furthermore, the recent introduction of digital material creator (DMC) add-ons to MMJ software allows for more streamlined creation of custom DMs. Thus, comparison of multi-material composite mechanical performance based on both geometric distribution and volumetric ratio of constituent materials warrants investigation. The purpose of this work was to determine structure-performance relationships for multi-material composites created using MMJ by systematically altering both the geometric distribution and volumetric ratio of materials.

We first assess the monotonic tensile properties of the base materials used in the composite creations: the "Vero" strong and rigid family and the "Agilus" soft and ductile family of PolyJet materials. We then design and manufacture composites with various geometric distributions of the two base materials including multilayered composites, sandwich composites, and voxel-scale designed custom DM composites. The specimens printed with these composite designs are tested monotonically in tension to gather mechanical performance data. Then, after printing and testing PolyJet preset DM composites available through the "Digital Material" library, we conclude with an assessment of mechanical performance and relative effect of geometric distribution for all composite designs based on volumetric ratio of rigid Vero to soft Agilus.

2. Materials and methods

2.1. Base materials

As demonstrated in Fig. 1, numerous mechanical properties are achievable using the PolyJet MMJ technology. The manufacturer printing software used for setting up build plates and printing on various Stratasys printing machines, GrabCAD Print, enables the user to assign single materials or preset DMs to the individual parts within the build plate. Of the collection of materials offered by Stratasys, Vero materials are among the more stiff and strong materials while Agilus and Tango materials are flexible and ductile. The strength and stiffness of Vero materials make it a more frequent selection for load-bearing applications, and the printability of rigid materials is higher than that of flexible materials due to the compliance of flexible materials during the printing process. However, Vero materials are more brittle, with an elongation at break around 5 %–20 % (Table 1). This makes an Agilus or Tango material a more suitable candidate where low stiffness or ductility is needed. Given the drastic difference in mechanical properties between the rigid (RM) and soft (SM) families of materials (Table 1), which are two of the most used material families for the J750 printer [17,21,22,24,25,49], one material from each family was selected for creating the composites: VeroMagenta (RM) and Agilus30Clear (SM). Manufacturer datasheets demonstrate a negligible difference in mechanical properties for materials of the same family but with different colors.

2.2. Composite specimen design

The cloud based Onshape CAD software was utilized to generate ASTM Type V "dogbones" as per ASTM D638. This standardized geometry was used for printing all composite specimens. After creation of the digital 3D model of a standardized dogbone specimen, additional steps were taken to create the different composite designs. Four composite designs were chosen for the study: multilayered (LAY) consisting of alternating layers of the two constituent materials, sandwich (SND) consisting of an interior layer of one material positioned between exterior layers of the other material on either side, customized digital materials (custom DM), and preset digital materials (preset DM) (Fig. 2). The LAY and SND designs were chosen due to their common use in composite applications such as materials covered in thin films [50,51], epoxy resin laminates [52,53], and polymer-based dielectrics [54,55].

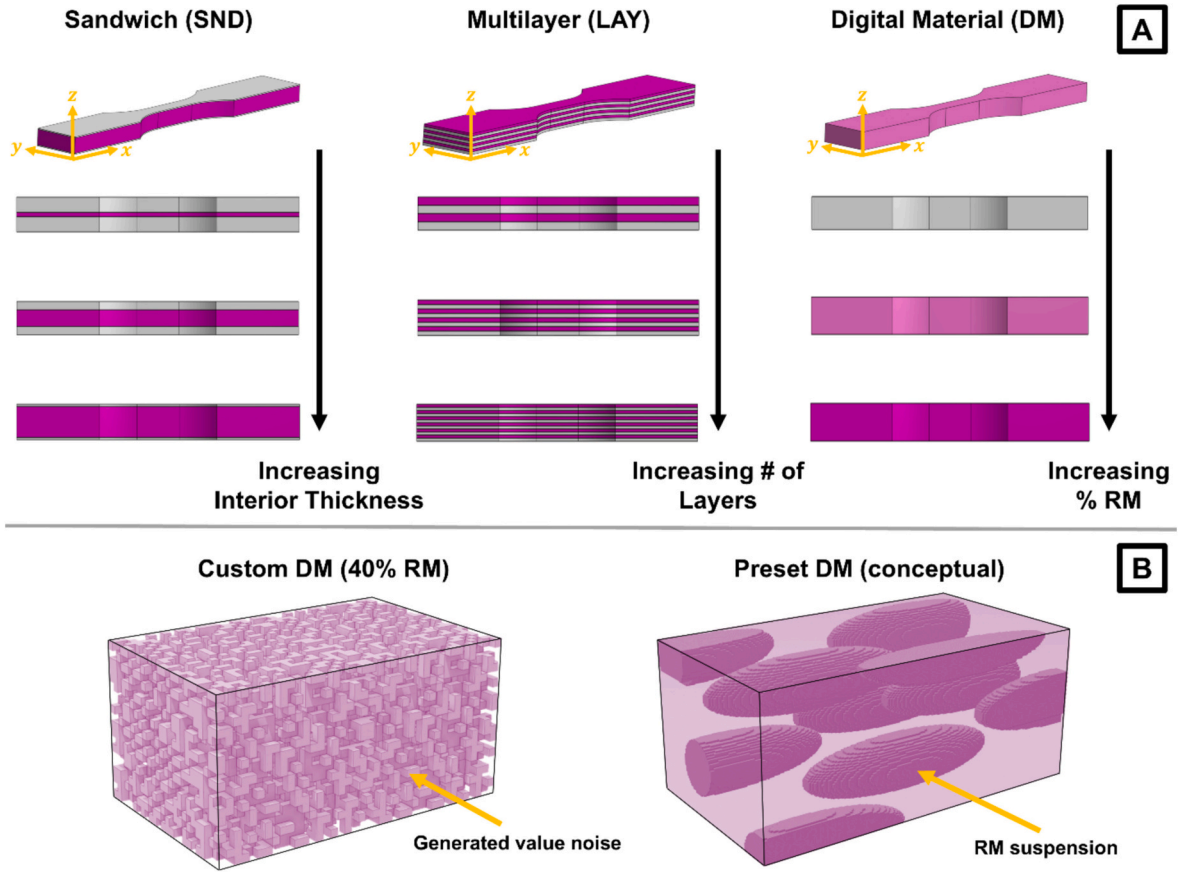

Fig. 2. Visualization of specimen geometry and composition range (A). The lighter color represents RM and the darker color represents SM. A zoomed-in view of the voxel distribution pattern of a custom DM and conceptual preset DM are displayed (B).

Table 2
Geometric and material parameters of printed test specimens. Five duplicate samples were created for each composite design to capture variance of the mechanical testing data.

Composite type	# of layers	Layer thickness [mm]	Material assignment
Base	1	solid	100 % RM or SM
Multilayer (LAY)	4, 6, 8, 10, 12	1, $0.6\overline{6}$, 0.5, 0.4, $0.3\overline{3}$	Alternating RM and SM layers
Sandwich (SND)	3	0.5, 1.0, 1.5, 2.0, 2.5, 3.0, 3.5	RM sandwiched between SM
		0.5, 1.5, 2.5, 3.5	SM sandwiched between RM
Custom DM	1	solid	10 % to 90 % RM or SM
Preset DM	1	solid	FLXA-MT-S##-DM
			##: 35, 40, 50, 60, 70, 85, 95

The LAY designs differ from the SND designs in that all LAY designs contained the same 1:1 volumetric ratio of RM to SM (Table 2). Thus, the LAY designs were included in the study to investigate the relative size effects of layer thickness on mechanical performance of layered composites produced using MMJ. Custom DMs were designed within the digital material creator (DMC) to compare against layered composites and preset DMs with respect to volumetric ratio of constituent materials. The specific processes for creating each composite design and DM within the DMC are detailed below.

For the LAY composites, the dogbone was divided along the thickness (z) dimension into layers such that the thickness of each layer multiplied by the number of layers of the specimen would equal 4 mm (Table 2). RM and SM materials were assigned to these specimens in an alternating layer fashion resulting in a total of five different LAY composites. The material distribution of RM and SM was defined within the DMC by the function:

$$f(z) = \begin{cases} 1, z \bmod \frac{2T}{N} \geq \frac{T}{N} \\ 0, z \bmod \frac{2T}{N} < \frac{T}{N} \end{cases} \quad (1)$$

where z is the vertical position along the thickness axis of the dogbone (Fig. 2A), T is the total thickness of the specimen, N is the number of layers within the specimen, and function f values of "0" and "1" indicate a material assignment of RM and SM, respectively.

For the SND composites, the specimen was divided along the thickness (z) dimension into three layers (Fig. 2A). Composites with varying interior layer thickness were created such that the exterior layers were of equal thickness, and when added together with the interior layer thickness, a total thickness of 4 mm would be achieved (Table 2). In the manufacturer software, RM and SM were assigned to the layers such that a "sandwich" of either Rigid-Soft-Rigid or Soft-Rigid-Soft was created for each of the interior thickness values listed in Table 2, resulting in a total

of eleven different SND composites. This "sandwiching" was achieved with a function defining the distribution of the RM and SM materials in the DMC:

$$f(z) = \begin{cases} 0, z < \dfrac{T - T_i}{2} \\ 1, \dfrac{T - T_i}{2} \le z \le T - \dfrac{T - T_i}{2} \\ 0, z > T - \dfrac{T - T_i}{2} \end{cases} \quad (2)$$

where z is the vertical position along the thickness axis of the dogbone (Fig. 2A), T is the total thickness of the specimen, T_i is the desired thickness of the inner layer, and function f values of "0" and "1" indicate RM and SM, respectively. For SND composites with RM as the interior material, the values for "0" and "1" are flipped within Eq. (2).

For the DM composites, the entire dogbone structure was assigned one of the available preset combinations of RM and SM (preset DM) available in GrabCAD Print or a custom-designed combination of RM and SM (custom DM) created using the DMC. The preset DMs are accessible through the "Digital Material" database in the manufacturer software, and a total of seven preset DMs with a Shore hardness range of 35 A to 95 A were possible by combining RM and SM (Table 2). Although the specific algorithm used to create the preset DMs is proprietary and not shared by Stratasys [34,45], Mueller et al. was able to determine the geometric distributions of preset DMs based on microscopic images of printed specimen surfaces and confirmed that they consist of ellipsoidal inclusions of one constituent material suspended within a matrix of the other material [56]. Furthermore, Slesarenko et al. devised a method for determining the volumetric ratios within preset DMs by analyzing material usage calculations in the printing software [49]. Calculated volumetric ratios of RM to SM for preset DMs and a conceptual 3D representation of a preset DM are presented in Table 3 and Fig. 2, respectively.

The custom DMs were composed of nine volume ratios of RM (%RM) between 10 % and 90 % in 10 % increments for a total of nine unique composites. The DMC software add-on was used to create all custom DMs, which were designed to create more homogenous mixtures of the constituent materials (Fig. 2B). Conversely, the preset DMs are more heterogenous in nature, containing ellipsoidal inclusions of RM material suspended in a matrix of SM (Fig. 2B). To create the custom DM material distribution, value noise was generated across the voxels of the CAD model bounding volume. Thresholds were then created for assigning the voxels to a specific material, in this case either RM for positive values or SM for negative values. To ensure that the correct ratio of RM to SM was achieved, a mean value constraint was placed on the noise generation such that the correct number of voxels was generated for each material. A list of the precise material distribution for each composite is available in Table S1 of the Supplementary materials [57].

2.3. Fabrication and post-processing

The ASTM tensile specimen models were imported into the manufacturer software, GrabCAD Print, to assign materials and orient the specimens on the build plate. The RM and SM materials (Vero and Agilus) were selected in the software and physically added to the J750 printer. Preset DMs were assigned to a subset of specimens by selecting combinations of RM and SM from the "Digital Material" library (Table 3). To create the custom DMs, LAY composites, and SND composites, RM and SM were selected within the DMC software and assigned to the voxels of remaining specimens using the methods described in Section 2.2. To keep printing conditions consistent against other MMJ studies, many of the following practices were adopted from Lumpe et al. [45] and Mueller et al. [58]:

- A nozzle clog test was performed following manufacturer guidelines prior to each print.
- Specimens were positioned evenly spaced from each other (20 mm).
- Specimen layout was automated with specimens placed as close to the printing platform origin (upper left) as possible while preserving 20 mm spacing.
- All specimens were oriented on the printing platform with tensile loading direction along the x-axis.
- To account for clogged nozzle effects, specimens varied in their y-axis coordinate such that no two specimens were aligned horizontally along the x-axis.
- Base materials from the same batches of identical expiry date were used.
- The printing nozzle was cleaned with isopropanol before the print.
- All specimens were printed with the "matte" print option.
- All specimens were stored in a dark place that is air-conditioned to room temperature ($T = 23$ °C).
- A default printing layer height of 27 μm was used.

Following the printing process, the specimens were removed from the build plate and allowed to soak in a warm water bath for 24 h. This allowed for the support material to break free from the specimens and avoided the risk of damaging specimen surfaces during manual support removal. The specimens were then allowed to dry completely for 24 h before mechanical testing. Printed specimens from each composite are presented in Fig. 3.

2.4. Mechanical testing and property extraction

To conduct uniaxial tensile testing, a TestResources® 910LX25 testing machine was used with a 25kN load cell. These tensile tests were conducted as per ASTM D638 standards, and repeatability of results was verified by testing five replicas per composite design. After the raw force and displacement data had been collected, it was then imported into MATLAB for further analysis. A custom MATLAB script was used to convert the force and displacement data into engineering stress and engineering strain, calculate mechanical properties of interest such as Young's modulus and yield strength, and plot stress-strain curves for each specimen [59]. Specific properties extracted from the curves were Young's modulus, ultimate tensile strength, and elongation at break. Raw data files for all specimens are available in the Supplementary

Table 3
Calculated material usage and volumetric ratio of RM to SM for preset DM composites.

Preset DM name	Shore hardness	Mass of RM used	Mass of SM used	Volumetric % RM
FLXA-MT-S35-DM	35A	24 g	292 g	7.6 %
FLXA-MT-S40-DM	40A	26 g	290 g	8.2 %
FLXA-MT-S50-DM	50A	29 g	287 g	9.2 %
FLXA-MT-S60-DM	60A	35 g	281 g	11.1 %
FLXA-MT-S70-DM	70A	46 g	270 g	14.6 %
FLXA-MT-S85-DM	85A	76 g	240 g	24.1 %
FLXA-MT-S95-DM	95A	107 g	209 g	33.9 %

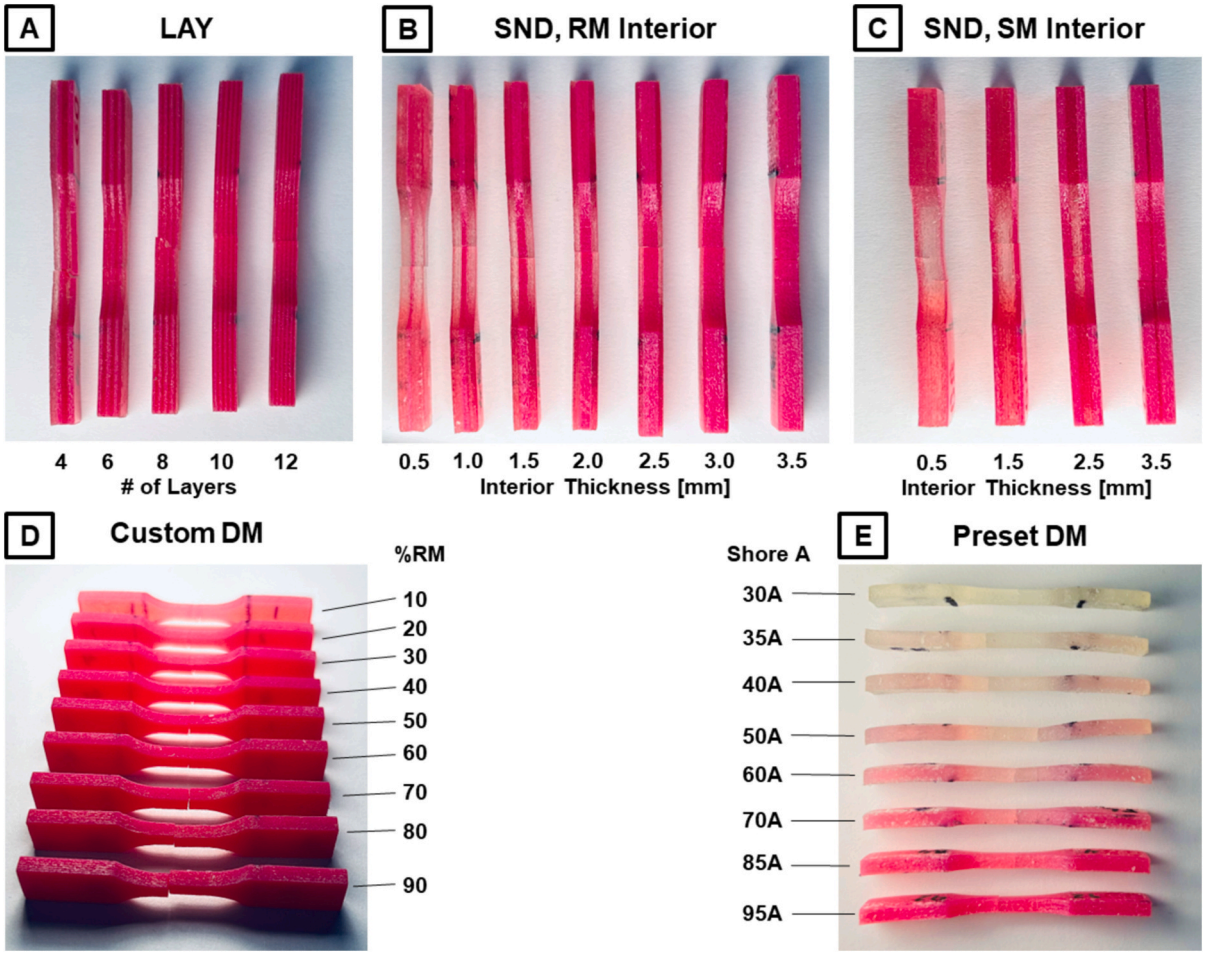

Fig. 3. Printed specimen examples for each composite. Specimens are organized into composite design groups LAY (A), SND with RM as interior material (B), SND with SM as interior material (C), custom DMs (D), and preset DMs (E). The pink material is RM and the clear material is SM. (For interpretation of the references to color in this figure legend, the reader is referred to the web version of this article.)

materials [57].

2.5. Finite element simulation

The open-source CalculiX finite element package was used to perform all computational analysis, with pre- and post-processing performed in the Windows-based graphical user interface (GUI) PrePoMax v2.0.0. The elasto-plastic behavior of the material was modeled with the Ramberg-Osgood law:

$$E\epsilon = \sigma + \left[\alpha\left(\frac{|\sigma|}{\sigma_0}\right)^{n-1}\right]\sigma \tag{3}$$

where E is the material Young's modulus, ϵ is the logarithmic strain, σ is the Cauchy stress, σ_0 is the yield stress, α is the yield offset, and n is the strain-hardening exponent. These material-specific values were determined for RM and SM by fitting the model to stress-strain curves gathered for 100 % RM and 100 % SM samples using the methods and custom MATLAB script described in Section 2.4. For all elements, second order ten-node tetrahedral elements were used (C3D10). Simulations were performed on a dedicated lab computer with an Intel Core i9-13900K Desktop Processor, NVIDIA GeForce RTX 4070 Ti SUPER graphics card, and 32GB of RAM. The nonlinear system of equations was solved using the PaStiX parallel solver across 12 cores [42,44].

3. Results

3.1. Base material results

Using the process outlined in Section 2.4, the base material RM and SM dogbones underwent tensile testing to produce stress-strain curves and extract desired mechanical properties (Table 4). The experimental data for RM displayed a Young's modulus of 1964 MPa, an ultimate tensile strength of 49 MPa, and an elongation at break of 9 %. These results show ultimate strength and elongation at break values consistent with those reported by the manufacturer in Table 1, while the experimentally determined Young's modulus value of 1964 MPa was less than the reported value. Experimental data from testing SM resulted in

Table 4
Experimentally determined mechanical properties of SM and RM materials. Shore hardness was determined using a calibrated durometer. Five duplicate samples were tested to capture variance of the property measurements.

Material name	Young's modulus [MPa]	Ultimate strength [MPa]	Elongation at break [%]	Shore hardness
Rigid Material(RM)	1964 ± 161	49 ± 4	9 ± 2	83D–87D85 ± 2
Soft Material (SM)	0.55 ± 0.06	0.78 ± 0.03	118 ± 10	27A–33A±3

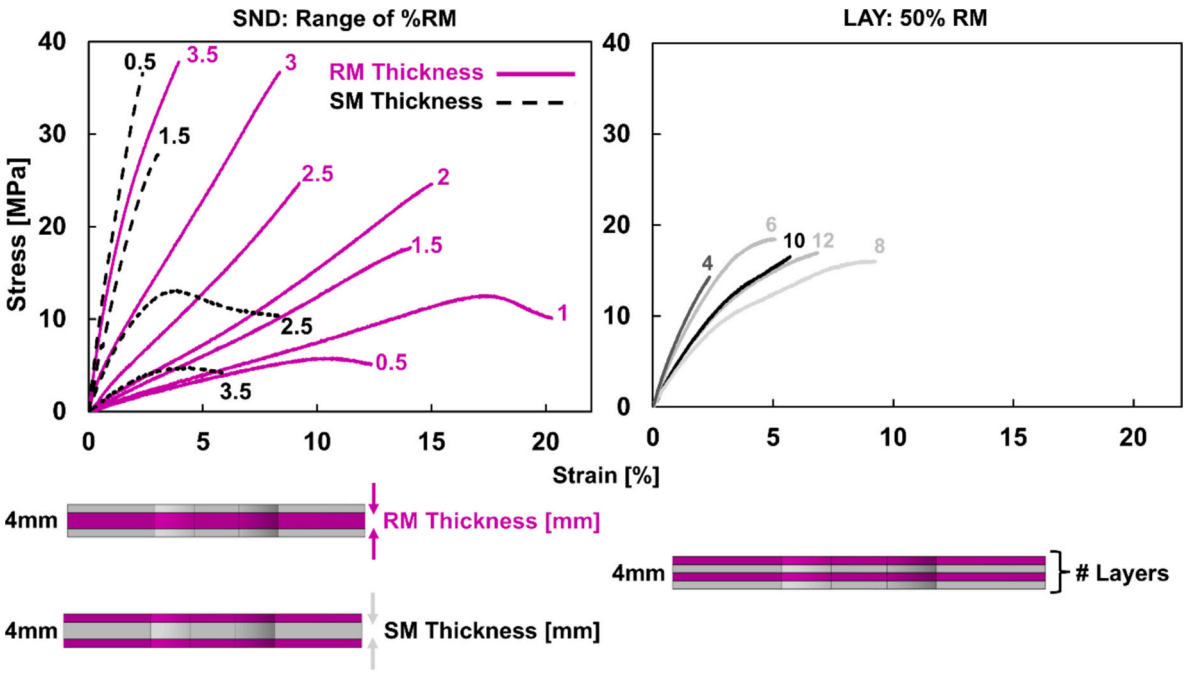

Fig. 4. Representative stress-strain curves for each SND composite (Left) and LAY composite (Right) design. For SND composites, the behavior of the curves as the interior portion thickness is increased is highly dependent on which material is in the interior portion. For the LAY composites, no uniform trend is observed based on the number of layers in the composite, although the ultimate strength remains relatively consistent.

Young's modulus of 0.55 MPa, ultimate strength of 0.78 MPa, and elongation at break of 118 %. While the Young's modulus of SM is not reported by the manufacturer, the experimental values of ultimate strength and elongation at break for SM are less than half the magnitude of those reported.

3.2. Layered composite results

3.2.1. Multilayer design results

Representative stress-strain curves for all LAY designs are displayed on the right panel of Fig. 4. For Young's modulus, the 4-layer design exhibited the highest average value at 711 MPa and the 8-layer design exhibited the lowest average value at 359 MPa. The highest average value for ultimate tensile strength was approximately 17 MPa for the 6-layer design, and the lowest was approximately 15 MPa for the 4-layer design. The elongation at break had the highest average value around 10 % for the 8-layer design and lowest around 2 % for the 4-layer design. For layer thickness values of each LAY composite, see Table 2.

3.2.2. Sandwich design results

In contrast to the LAY composites, the recorded mechanical properties of the SND composites show clearer trends with increased %RM (Fig. 4). As the thickness of the stiffer RM interior layer increased from 0.5 mm to 3.5 mm, the Young's modulus increased by a factor of 23.4 from 58 MPa to 1360 MPa, the ultimate strength increased by a factor of 6.2 from 6 MPa to 37 MPa, and the elongation at break decreased by a factor of 3.4 from 17 % to 5 %. Conversely, as the thickness of the softer SM interior layer increases from 0.5 mm to 3.5 mm, the properties show opposite trends with a decrease in Young's modulus by a factor of 9.5 from 1800 MPa to 190 MPa, a decrease in ultimate strength by a factor of 7.8 from 31 MPa to 4 MPa, and an increase in elongation at break by a factor of 4 from 2 % to 8 %. These observations are logical due to the higher volume ratio of stiff versus soft material as the RM interior layer thickness is increased or the SM interior layer thickness is decreased. Interestingly, however, SND composites with the same volume ratio of RM show nearly double the elongation at break when RM is used as the interior layer material.

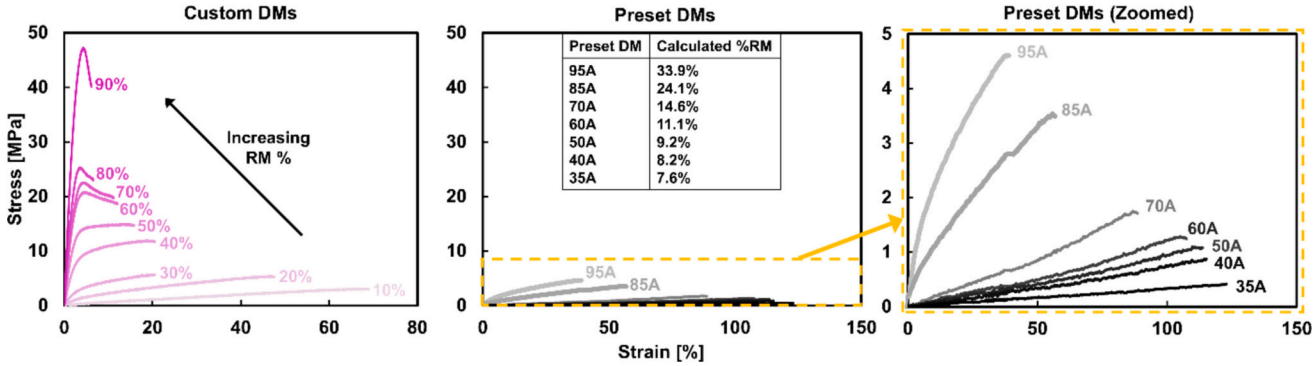

Fig. 5. Representative stress-strain curves for custom and preset DM composites. The volume ratio of RM versus SM is increased from 10 % to 90 % in increments of 10 % for the custom DMs designed using the DMC software (Left). Preset DMs containing RM and SM in the manufacturer software with varying shore hardness from 35 A to 95 A were printed and tested to compare to the custom DMs (Middle, Right).

3.3. Preset and custom DM results

Compared to using manufacturer preset DMs containing RM and SM, using the DMC to create custom DMs resulted in composites with a much larger range of mechanical performance (Fig. 5). The custom DMs achieved a range of 5 MPa to 1862 MPa for Young's modulus, 3 MPa to 44 MPa for ultimate strength, and 5 % to 69 % for elongation at break. Conversely, the preset DMs achieved a range of 1 MPa to 32 MPa for Young's modulus, 1 MPa to 5 MPa ultimate strength, and 38 % to 111 % for elongation at break. The calculated %RM values for preset DMs presented in Table 3 show that the highest %RM allowable for these composites is approximately 34 % compared to 90 % in the custom DMs. Thus, an interesting comparison can be made between custom and preset DMs with similar %RM. Upon examination of Fig. 5, at similar % RM the custom DMs tend to exhibit greater Young's modulus and ultimate strength, while preset DMs show an advantage in elongation at break. These results and their implications are discussed further in Section 4.4.

4. Discussion

4.1. Base materials discussion

While the significant difference in properties between RM and SM is evident in both the reported data by the manufacturer in Table 1 and the experimentally gathered data in Table 4, there were notable discrepancies between reported versus experimental properties. Namely, experimental values for SM ultimate strength, SM elongation at break, and RM Young's modulus were all significantly lower than those reported by the manufacturer. In a study conducted by Ruiz et al., in collaboration with the manufacturer, they recorded an average ultimate strength of 2.4 MPa for SM [60]. However, they used ASTM D638 Type IV dogbones and a testing rate of 50 mm/min, while in this study ASTM D638 Type V dogbones were tested at a rate of 10 mm/min. Testing at a faster rate will typically result in larger recorded strength and stiffness for elastic, ductile materials [61]. Additionally, while the manufacturer reports a Young's modulus of between 2200 and 3000 MPa for RM, research led by Su et al. reported a Young's modulus of 1220 MPa [62]. This value correlates with the value of 1964 MPa obtained in this study, thus validating a lower value than the manufacturer's reported value. Nevertheless, the unique advantage of MMJ is the ability to print materials with a wide range of mechanical properties on the same print bed with a high degree of resolution, and both the manufacturer-reported and experimentally determined results highlight this advantage regardless of their discrepancies.

4.2. Multilayer design discussion

Upon examination of the stress-strain curves for LAY composites in Fig. 4, maintaining a constant volume ratio of constituent materials and increasing the relative layer thickness appears to have a slight effect on both Young's modulus and elongation at break, and a minimal effect on ultimate tensile strength. This conclusion is further verified by the trends observed in Fig. 7. With respect to increasing layer thickness, Young's modulus shows a positive correlation (Fig. 7D), elongation at break shows a negative correlation (Fig. 7E), and ultimate strength shows no correlation (Fig. 7F). The variance in Fig. 7E suggests that the negative correlation between layer thickness and elongation at break may be stronger than it appears in Fig. 4.

Interestingly, similar trends as these have been observed for FFF-fabricated tensile specimens with varying layer thickness. Numerous studies have shown minimal effect of relative layer thickness on ultimate tensile strength [63–66], and Samykano et al. also documented a positive correlation between Young's modulus and layer thickness for 3D printed acrylonitrile butadiene styrene (ABS) [64]. Furthermore, Somireddy et al. found a positive correlation for Young's modulus and a negative correlation for elongation at break with respect to layer thickness in printed ABS composites [66]. Although FFF and MMJ are entirely different printing technologies, altering the layer thickness of extruded filament in FFF or composite layer thickness in these LAY composites affects the total interfacial surface area between layers in both cases.

For layered composites not manufactured using AM, prior studies show a significant degree of delamination contributing to eventual failure of tensile specimens [67–72]. This is particularly the case for composites created using dissimilar materials, such as metal-polymer composites, where adhesion between layers often lacks a chemically created bond [73,74]. Conversely, in the case of layered composites created using MMJ, intermittent photopolymerization during printing from ultraviolet curing light can create chemical bonds across the interface between layers, which strengthen the bond between layers and prevent delamination.

4.3. Sandwich design discussion

The stress-strain curves measured for the SND composite stress-strain curves in Fig. 4 demonstrate stronger relationships than the LAY stress-strain curves. The ultimate strength of SND composites were far more impacted by the change in %RM versus layer thickness in the LAY composites. The difference in ultimate strength between SND composites with rigid (RM) versus soft (SM) material as the interior layer was minimal. However, composites with a soft interior layer failed to achieve the same degree of elongation at break as the RM interior composites (Fig. 4). This difference could be attributed to the interface between the testing grips and the different exterior layer materials of the two composite groups (Fig. 3B, C). With SM exterior material, slipping may have occurred at the interface which would delay the true elongation and eventual fracture of the composite. However, no visible slipping occurred when examining the stress-strain curves or grip-contacting surfaces of the specimens after testing. Another consideration is that the shear deformation between the grip interface and the layer interfaces would be greater for composites with SM exterior layers. As such, the RM interior layer of the composite would not experience a tensile force until shear deformation had stopped for the SM exterior layers.

To validate this hypothesis, computational analysis of tensile performance for various SND composites was performed using finite element analysis (FEA) following the methods in Section 2.5. New CAD designs were made with 100 % RM tab portions to interface with the grips (Fig. 6A), and monotonic tensile simulations were run on the original experimental designs and modified designs (Fig. 6B, C). Simulation results for the original designs aligned well with the experimentally gathered results, demonstrating that the computational analysis framework could produce accurate results. For the SM interior composites, the addition of 100 % RM tabs had little to no effect on the mechanical properties (Fig. 6C), however the RM interior composites showed a significant increase in Young's modulus (Fig. 6B). Thus, it is likely that the discrepancy between SM interior and RM interior Young's modulus for SND composites was due to shear deformation within the softer exterior layers of the RM interior composite. Future experiments may account for this by taking advantage of the multi-material capabilities of the J750 and printing only the gauge section as the composite material, such as the designs in Fig. 6A.

4.4. Volumetric material ratio and distribution comparison

In Fig. 7A, B, C the mechanical property trends of the different composite geometries and DMs with respect to changes in volume %RM are displayed. As discussed in Section 4.3, the RM interior SND composites exhibited lower Young's modulus elongation at break than other composites due to the soft material interface at the grip face. The Young's moduli of RM interior SND composites were dominated by the

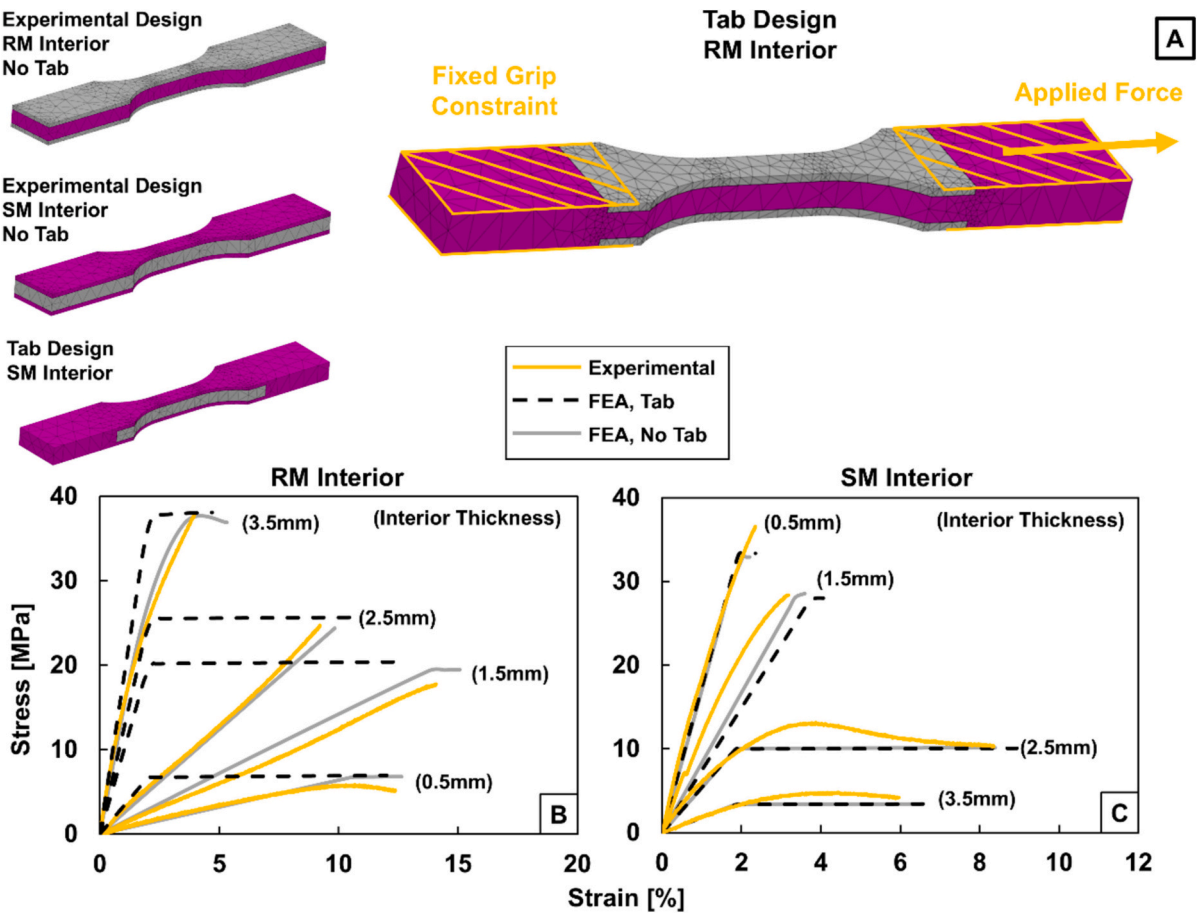

Fig. 6. CAD models used in FEA simulations to validate grip contact material effects for SND composites (A). Monotonic tensile test simulations are performed with original experimental SND composite designs and modified designs with tabs made from rigid RM material for interfacing with the testing grips. Simulation results for both designs are compared to the experimentally gathered results for RM interior (B) and SM interior (C) SND composites.

properties of SM until a sufficiently high %RM was used such that the soft interface layer shear deformation was thin and minimally impactful, and the modulus was dominated by RM. Consequently, an exponential behavior was displayed for the RM interior SND composites in Fig. 7A. The same shear deformation that caused this discrepancy in Young's modulus caused the elongation at break of the RM interior composites to be artificially higher than the SM interior (Fig. 7B). As verified by the computational analysis discussed in Section 4.3, creating rigid tabs on RM interior samples would result in SND composite specimens with similar mechanical properties at fixed %RM regardless of which material is interior versus exterior (Fig. 6A, B).

The discrepancies between preset DM and custom DM mechanical properties at fixed %RM can be explained by examination of the voxel-scale distribution of material between the two types of DM. At fixed % RM, preset DMs contain lower Young's modulus and ultimate strength but higher elongation at break than custom DMs (Fig. 7A, B, C). The nature of the ellipsoidal inclusions in the preset DMs create a high degree of *continuous* interfaces between the constituent materials, however the voxel-scale material distribution in the custom DMs creates a higher overall interfacial area between constituent materials (Fig. 2B). It is well established that a higher interfacial area will result in better stress transfer between the inclusions and matrix and ultimately improved composite strength [38,75,76] (Fig. 7C). Additionally, the smaller "particle size" of the voxel-scale material distribution in the custom DMs compared to the ellipsoidal inclusions in preset DMs exhibits a critical particle size effect where the composite stiffness is greatly enhanced [75] (Fig. 7A). As for elongation at break, the more continuous interfaces within the preset DMs provide a reduced degree of stress concentrations which are known to contribute to premature brittle fracture (Fig. 7B). Of these considered effects, the enhanced stiffness of the custom DMs compared to preset DMs is most significant, with an increase of as much as a factor of 8 at 35 % RM (Fig. 7A).

The trends observed for the LAY composites can be described by the constituent material interfaces as well. Due to the laminate nature of the LAY composites, increasing the number of layers results in an increased overall interfacial area; however, for monotonic tensile testing the interfaces are all oriented parallel to the testing direction (Fig. 3A). At these interfaces, shear forces between layers occur as the higher stiffness of RM layers deters them from displacing as much as SM at a given applied force. Consequently, an uneven distribution of deformation occurs within the sample depending on the thicknesses and differences in material properties between layers. Further investigation of this consequence is discussed in Sections 4.5 and 4.6.

Fig. 7 demonstrates that by using a custom voxel-scale design, composites with mechanical properties spanning the entire range of the individual constituent materials are achievable. This gives the user the ability to utilize the full capabilities of MMJ by using a property first, material prioritized mentality. If a particular property is needed, the DMC allows for that specific property to be reached by customizing the material distribution at the voxel scale, given that the property or properties are an aggregate of the constituent materials. The improved performance of these customized material distributions over other composite geometries is highlighted by examining the average modulus of toughness, or area under the stress-strain curve, for all sample groups. Namely, we see maximum achievable modulus of toughness values of 2.25, 1.15, 1.08, and 1.44 MPa for custom DMs, preset DMs, LAY

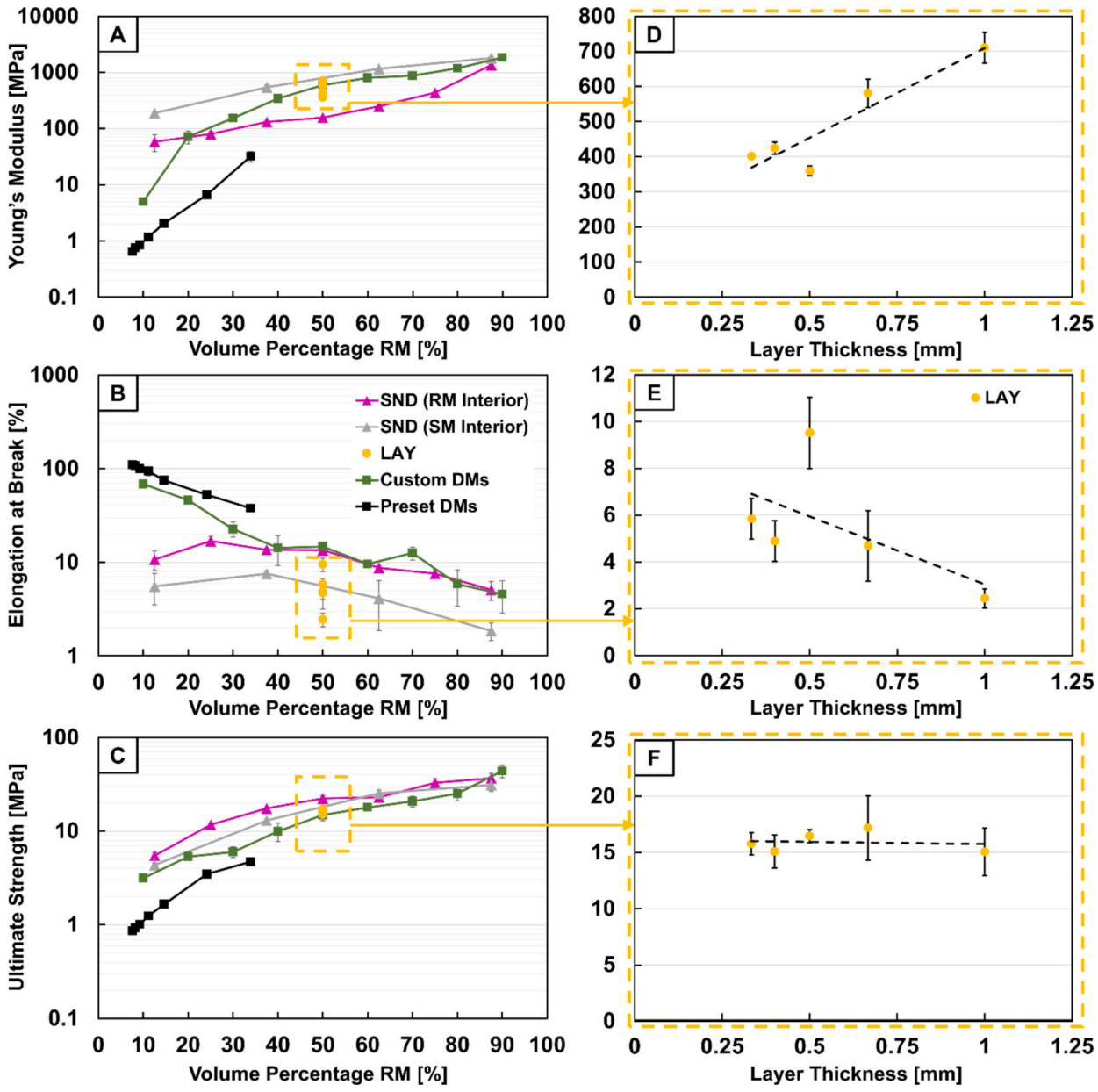

Fig. 7. Mechanical property trends with respect to change in %RM (A, B, C) and layer thickness (D, E, F) Changes in the measured Young's modulus, elongation at break and ultimate strength of LAY, SND, and custom DM composites are displayed in plots A, B, and C, respectively. All LAY composites were a 50–50 volumetric ratio of RM and SM, so changes in these three mechanical properties of LAY composites with respect to layer thickness are shown on a non-logarithmic scale in plots D, E, and F.

composites, and SND composites, respectively.

4.5. Morphological analysis and fracture mechanisms of multilayered composites

To better understand the trends observed for LAY composites, morphological analysis and computational simulation were performed to determine fracture and deformation mechanisms within these composites. Microscopic analysis of fracture surfaces in LAY composites highlighted the alternating sequential failure of layers from the outermost layers in contact with the grips toward the center of the specimen (Fig. 8A), with the outermost RM layer most consistently fracturing first. *Note that only half of the 12-layer fracture surface is displayed in* Fig. 8A, and that the second RM layer from the left would fail after both outermost RM layers on either side of the center have failed. Closer examination of the interface between RM and SM layers in Fig. 8C shows the brittle fracture energy of an RM layer propagating across the interface and causing tearing within the adjacent SM layer. Coupled with generally well-bonded interfaces between layers, this would explain the continuity of fracture lines across layers in Fig. 8D. In the absence of this tearing at the interface between layers, SM layers would remain intact and be free to continue deforming, creating disjoint fracture lines across the layers when SM finally fails. The interfacial bonding is highlighted in Fig. 8B, where the wave-like interface between RM and SM remains well-bonded after fracture.

To validate this hypothesis, computational analysis was performed to simulate mechanical loading of LAY samples (Fig. 9) using the same setup and procedure described in Section 2.5. One consideration for the analysis was to model the interface as wave-like to match that seen in Fig. 8B, a result of the voxel-scale material distribution as discussed in Section 4.4 and in previous work [33,37]. However, capturing these features with tetrahedral finite elements while successfully modelling

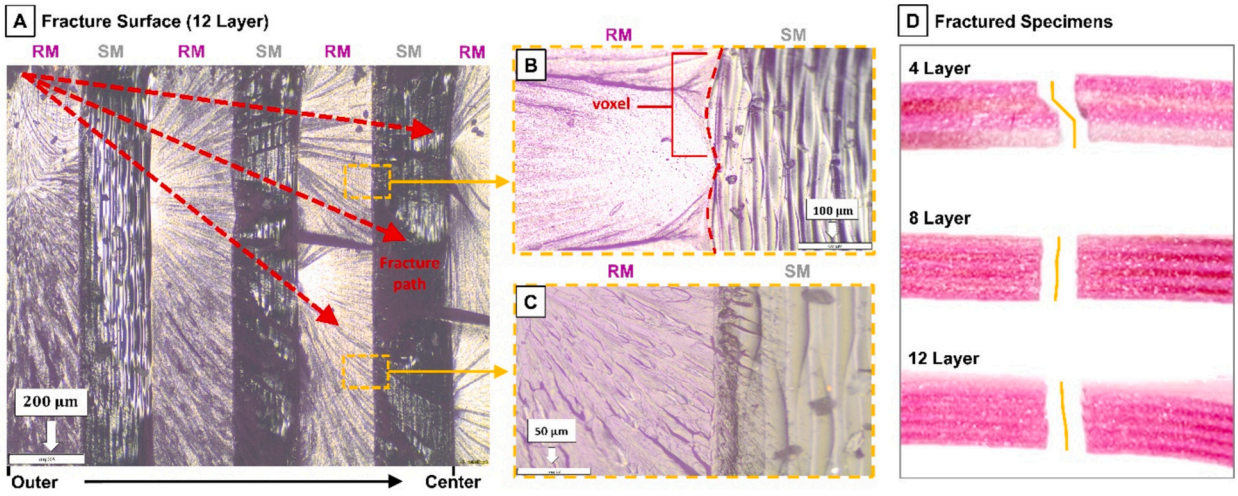

Fig. 8. Microscopic fracture surface and morphological analysis of broken LAY samples. An orthogonal microscopic view of a fractured 12-layer sample (A) shows the failure path originating on the exterior RM layer and extending toward the center, typical of all LAY samples. Strong bonding with minimal gaps between layers (B) and sudden brittle fracture of RM samples cause tearing and fracture propagation into adjacent SM layers (C). Fracture of initial outer RM sample layers creates an imbalance in the applied force for samples with less layers and leads to jagged fracture across layers (D).

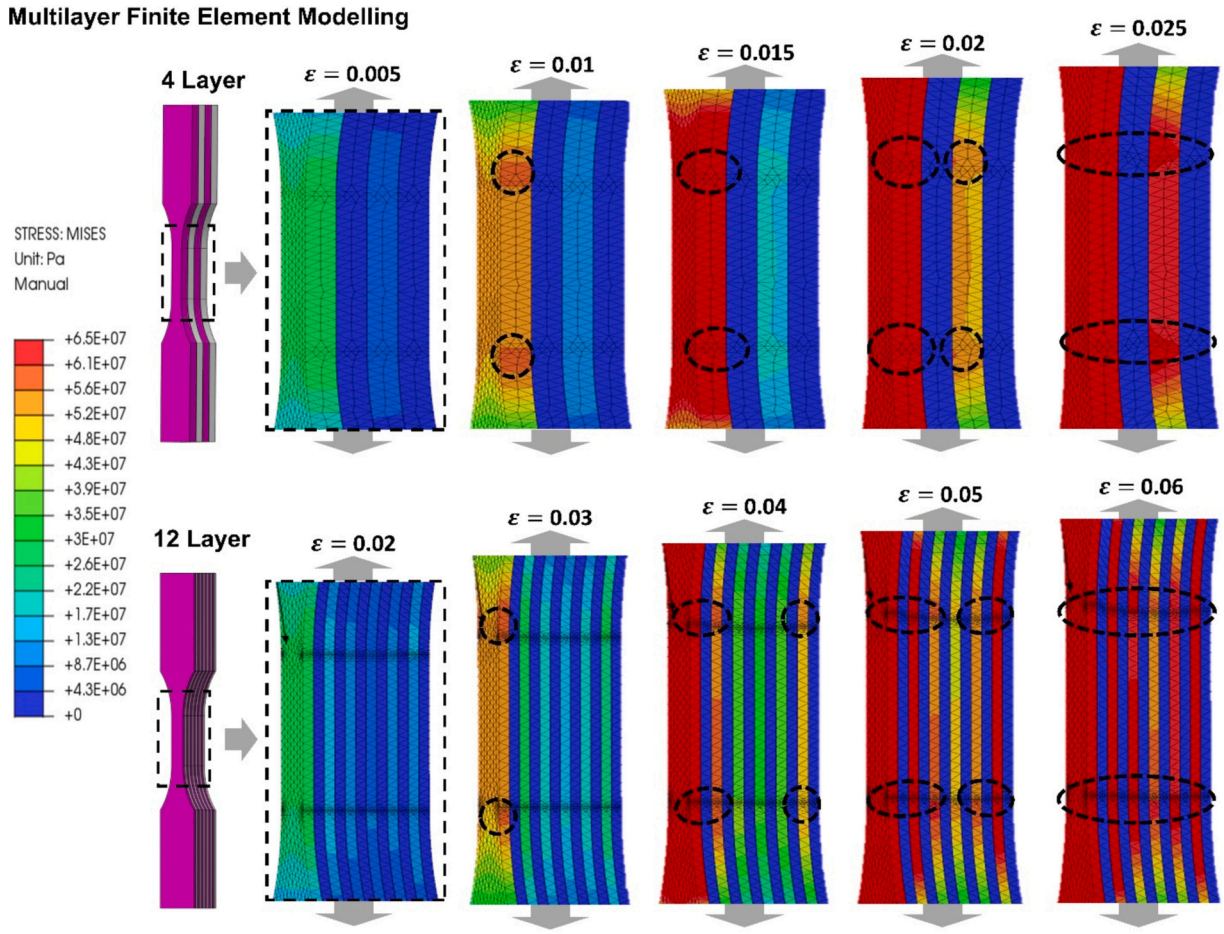

Fig. 9. Finite element analysis of LAY samples. The results for 4-layer and 12-layer samples are displayed, with deformation occurring axially along the sample and parallel to the orientation of the layers. Four distributed shear forces were created as boundary conditions to simulate the forces applied by the grips on the outermost sample layers (see Fig. 6). The analysis demonstrates the sequential high stress regions starting on the outermost layers and moving toward the center in an alternating fashion, dominated by the more rigid and stiff RM layers. Layers of SM have significantly lower elastic modulus and remain unstressed at lower displacement strain (dark blue layers). (For interpretation of the references to color in this figure legend, the reader is referred to the web version of this article.)

the entire multilayered sample would require millions of elements and exceptionally large amounts of computing power, and with the well-bonded nature of the interfaces already established it was decided to model the interface as a flat surface.

In future investigation, we propose modelling this wave-like interface and performing experimental and computational analysis on crack propagation to determine how stress concentrations form at the micro-scale and how interfacial material designs may be improved to account for this material deposition geometry.

As displayed in Fig. 9 by the dashed black ellipses, sequential failure of RM layers occurs from the outer-most to inner-most layers, which aligns with the fracture patterns observed on the sample fracture surfaces (Fig. 8A). For samples with less layers, such as 4, fracture of the first RM layer immediately creates an imbalance in the system as the center of mass is shifted toward the unbroken layers, resulting in a moment about the new center and the jagged fracture path observed in Fig. 8D. With more layers, the center of mass is shifted by less during each sequential layer break and a more linear fracture path is created.

The sequential fracture and tearing observed in Fig. 8D and C, respectively, provide insight into the trends in mechanical properties of layered samples observed in Fig. 7D–F. As the number of layers decreases and thickness of each layer increases, initial fracture of the outermost layer more significantly impacts the overall sample geometry and mechanical performance. In a 4-layer composite, one quarter of the sample fractures, causing an imbalance as described above (Fig. 8D). Furthermore, as the layer thickness increases, there is more energy dissipated due to fracture, and consequently more significant tearing is likely to occur in the adjacent layers (Fig. 8C). As demonstrated in Fig. 7E, these occurrences result in earlier and more instantaneous perceived failure of the composite compared to composites with more layers that tend to fail gradually. Conversely, increased layer thickness results in a higher Young's modulus due to the dominating behavior of the outermost RM layer prior to its fracture (Fig. 7D). The ultimate tensile strength remains relatively constant with increased number of layers as the same ratio of constituent materials must be fractured at any given cross-section (Fig. 7F).

While the mechanisms driving these trends are readily apparent in this case, these multilayer composite samples contain relatively simple geometry with only two materials in an alternating pattern and uniform layer thickness. To make informed performance predictions of arbitrary and more complex multilayer composites, an analytical model is presented in Section 4.6 for determining deformation due to tensile loading in multilayer composites.

4.6. Multilayered composite tensile deformation model

Multilayered composites exhibit complex deformation profiles and fracture behavior, particularly with composites containing three or more materials and uneven layer thicknesses. Based on the alternating sequential failure of layers in LAY samples and observations discussed in Sections 4.3 and 4.5, it was clear that uniform deformation did not occur within LAY or SND samples. Thus, a mathematical model was developed to calculate deformation along the axial loading direction (X in Fig. 10A), parallel to the composite layers, which depends upon vertical position within the sample (Z in Fig. 10A). The developed model is specific to the following loading scenario:

- Sample with total thickness T is fixed at the origin in the YZ plane (e.g., in Fig. 10A, at a slice orthogonal to the X direction and dissecting the LAY sample in half).
- Applied shear loads F_1 at the bottom surface ($z = 0$) and F_2 at the top surface ($z = T$) occur over area A and along the X direction.
- All other surfaces are free boundaries.
- A total of N layers with individual thickness t and material properties E and ν have a cumulative thickness equal to the total sample thickness T.

Given the loading scenario described above, the deformation along the X direction (u_x) at a given height within the sample (z), measured from the bottom surface, can be determined from the classical shear relationship in continuum mechanics:

$$G = \frac{\tau}{\gamma} = \frac{F/A}{u_x/t} = \frac{Ft}{Au_x} \rightarrow u_x = \frac{Ft}{GA} \tag{4}$$

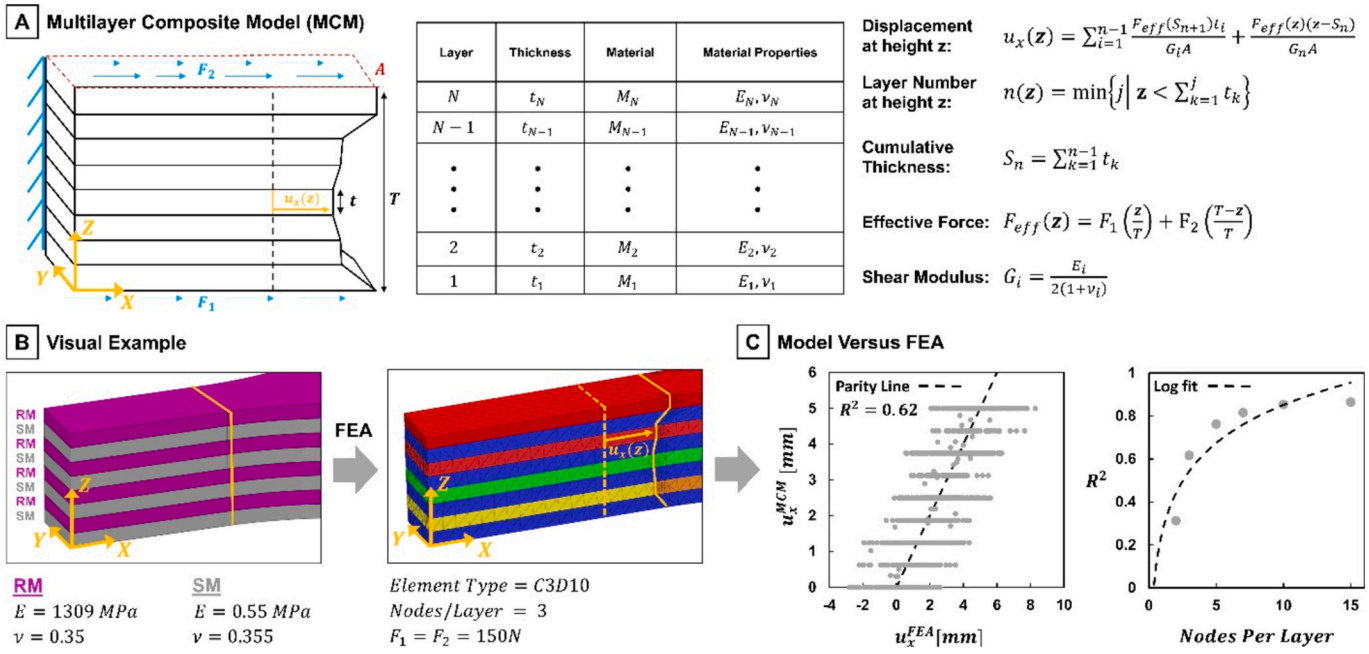

Fig. 10. Model framework for calculating displacement along the direction of loading within multilayered composite specimens. The boundary conditions (A) require that the composite be fixed at one end and have shear loading applied along the top and bottom surfaces. The system of equations can be solved using just the layer information contained in the table and the position along Z. An example comparing the model performance to FEA results is demonstrated for the 8-layer RM/SM composite tested in this study (B). Performance results between the model and FEA and with varying finite element nodes per layer are presented (C).

However, F and G are functions of height z in layered composite materials because the material properties are not uniform along the Z direction. Considering this, and using summative shear deformation, the following set of equations can be derived:

$$u_x(\boldsymbol{z}) = \sum_{i=1}^{n-1} \frac{F_{eff}(S_{n+1})t_i}{G_i A} + \frac{F_{eff}(\boldsymbol{z})(\boldsymbol{z} - S_n)}{G_n A} \tag{5}$$

$$n(\boldsymbol{z}) = min\left\{ j |\, \mathbf{z} < \sum_{k=1}^{j} t_k \right\} \tag{6}$$

$$S_n = \sum_{k=1}^{n-1} t_k \tag{7}$$

$$F_{eff}(\boldsymbol{z}) = F_1\left(\frac{\boldsymbol{z}}{T}\right) + \mathrm{F}_2\left(\frac{T - \boldsymbol{z}}{T}\right) \tag{8}$$

$$G_i = \frac{E_i}{2(1 + \nu_i)} \tag{9}$$

where $\boldsymbol{z}$ is the position along the Z direction, $\boldsymbol{n}$ is the layer at position z, $\boldsymbol{S_{n-1}}$ is the cumulative thickness of all layers up until layer n, $\boldsymbol{F_{eff}}$ is the effective shear force due to F_1 and F_2 at position z, and $\boldsymbol{G_n}$ is the shear modulus of layer n. For a full derivation of these equations, please see the Supplementary materials [57].

To quantify the performance of the proposed multilayer composite model (MCM), displacement calculations were compared to results from computational analysis performed on LAY samples (Fig. 10B). For these computational simulations, only linear-elastic properties of the material were used as the proposed MCM does not account for plasticity. Using the 8-layer composite FEA results, a randomized set of 5000 nodes was sampled from the finite element mesh. A custom MATLAB script and Eqs. (5)–(9) were then used to calculate the theoretical displacement in the X direction for each node and compare the values to the FEA results (Fig. 10C) [57]. In the original mesh with C3D10 tetrahedral elements, nodes were distributed such that each layer had a node on the top, bottom, and center, which lead to the stepwise appearance of the MCM versus FEA displacement plot in Fig. 10C. To see if the coarseness of the finite element mesh affected MCM performance, subsequent comparisons were made using FEA simulations with finer meshes and thus more nodes per layer. In the right plot of Fig. 10C the relationship between MCM performance (quantified using the coefficient of determination, R^2) and nodes per layer in the FEA follows a logarithmic trend that plateaus around an R^2 value of 0.85. With this level of performance for the MCM, the logical next step and future work would be to incorporate plasticity into the model and compare the calculated displacements to those from an elasto-plastic FEA simulation.

Existing literature contains extensive models on the mechanical behavior of multilayer composites, including studies on fiber-reinforced composites [41,77–80], bending [81–83], tension [84–87], and transverse shear behavior [88,89]. Classical Laminate Theory (CLT) is widely used for predicting stiffness and strength in traditional laminated composites assuming homogeneous material properties within layers. Shear-lag theory (SLT) models stress transfer between composite layers but typically requires continuous and uniform interfaces. However, these established models have limitations when applied to MMJ-fabricated composites. First, MMJ allows for voxel-scale material distributions within and across layers, leading to non-homogeneous layers that CLT cannot accurately model. Additionally, the UV-curing process in MMJ creates strong chemical bonds between layers, reducing the likelihood of delamination. Traditional models often account for weaker mechanical bonding and interfacial failures, which are not prevalent in MMJ composites. Furthermore, MMJ composites exhibit mixed-mode failures, including brittle fracture and tearing across layers, which are not adequately predicted by CLT or SLT.

As discussed in Section 4.2, non-AM layered composites frequently demonstrate delamination during uniaxial tensile testing, necessitating models that incorporate delamination effects. In contrast, the MMJ composites analyzed in this study did not experience delamination prior to fracture due to their strong interfacial bonds. Therefore, CLT and SLT require modifications to accurately predict the mechanical behavior of MMJ-fabricated layered composites. Our findings suggest that existing models should be adapted to 1) consider non-homogeneous material properties by incorporating voxel-scale variations within layers, 2) account for the chemical bonds formed during UV-curing in MMJ processes, and 3) handle materials with continuous variations in properties along both loading and transverse directions. Future work should focus on enhancing the MCM by incorporating plasticity and comparing its predictions with elasto-plastic FEA simulations. Additionally, developing new or modified theories that integrate the unique aspects of MMJ, such as voxel-scale design and enhanced interfacial bonding, will improve the accuracy of mechanical performance predictions and layered composite modelling.

5. Conclusions

The results of this study provide insight into the mechanical behavior of layered composites and voxel-scale designed digital materials printed using MMJ. Sandwich and multilayer composites helped illustrate the fundamental ways in which material distribution of two-material layered composites affect the mechanical properties of printed parts based on geometry and orientation of material interfaces. Analysis of custom digital material composites demonstrated that custom voxel-scale design provides better control over mechanical performance than traditional layered composites and increased Young's modulus and ultimate strength over the current manufacturer preset DMs. When paired with custom voxel-scale design, MMJ enables endless possibilities for material distribution and composition, leveraging the full range of capabilities of MMJ technology and enabling printing of previously unachievable geometries. This study investigated a small range of the possibilities for MMJ technology, and in future work, capabilities of this technology such as combinations of three or more materials, gradient designs for smoother and more continuous material interfacing, and architected materials such as lattice structures with customized material distributions will be explored using custom voxel-scale design.

CRediT authorship contribution statement

Niusha Daneshdoost: Writing – original draft, Visualization, Validation, Project administration, Methodology, Investigation, Formal analysis, Data curation, Conceptualization. **Jacob Peloquin:** Writing – review & editing, Visualization, Software, Formal analysis, Data curation. **Ken Gall:** Writing – review & editing, Supervision, Resources, Funding acquisition, Formal analysis, Conceptualization.

Declaration of competing interest

The authors declare that they have no known competing financial interests or personal relationships that could have appeared to influence the work reported in this paper.

Acknowledgements

We would like to acknowledge support from the Innovation Co-Lab at Duke University for providing access to a Stratasys J750 Digital Anatomy printer. The authors also acknowledge financial support from the National Science Foundation [DGE-2022040] and the National Science Foundation Graduate Research Fellowship Program.

Appendix A. Supplementary data

Supplementary data to this article can be found online at https://data.mendeley.com/datasets/ny3h2739hg/2.

Data availability

The data and code used for this study is available upon request.

References

[1] Wang B, Zhang Z, Pei Z, Qiu J, Wang S. Current progress on the 3D printing of thermosets. Adv Compos Hybrid Mater 2020;3:462–72. https://doi.org/10.1007/s42114-020-00183-z.

[2] Dizon JRC, Espera AH, Chen Q, Advincula RC. Mechanical characterization of 3D-printed polymers. Addit Manuf 2018;20:44–67. https://doi.org/10.1016/j.addma.2017.12.002.

[3] Ford SLN. Additive manufacturing technology: potential implications for U.S. Manufacturing Competitiveness. Journal of Commerce and Economics 2014;1:1–35. https://ssrn.com/abstract=2501065.

[4] Jiang Z, Diggle B, Tan ML, Viktorova J, Bennett CW, Connal LA. Extrusion 3D printing of polymeric materials with advanced properties. Advanced Science 2020;7:2001379. https://doi.org/10.1002/advs.202001379.

[5] Shahrubudin N, Lee TC, Ramlan R. An overview on 3D printing technology: technological, materials, and applications. Procedia Manuf 2019;35:1286–96. https://doi.org/10.1016/j.promfg.2019.06.089.

[6] Herzberger J, Sirrine JM, Williams CB, Long TE. Polymer design for 3D printing elastomers: recent advances in structure, properties, and printing. Prog Polym Sci 2019;97:101144. https://doi.org/10.1016/j.progpolymsci.2019.101144.

[7] Han W, Kong L, Xu M. Advances in selective laser sintering of polymers. International Journal of Extreme Manufacturing 2022;4:042002. https://doi.org/10.1088/2631-7990/ac9096.

[8] Levy GN, Schindel R, Kruth JP. Rapid manufacturing and rapid tooling with layer manufacturing (lm) technologies, STATE of the art and future perspectives. CIRP Annals 2003;52:589–609. https://doi.org/10.1016/S0007-8506(07)60206-6.

[9] Mehrpouya M, Tuma D, Vaneker T, Afrasiabi M, Bambach M, Gibson I. Multimaterial powder bed fusion techniques. Rapid Prototyp J 2022;28:1–19. https://doi.org/10.1108/RPJ-01-2022-0014.

[10] Ge Q, Chen Z, Cheng J, Zhang B, Zhang Y-F, Li H, et al. 3D printing of highly stretchable hydrogel with diverse UV curable polymers. Sci Adv 2021:7. https://doi.org/10.1126/sciadv.aba4261.

[11] Kowsari K, Akbari S, Wang D, Fang NX, Ge Q. High-efficiency high-resolution multimaterial fabrication for digital light processing-based three-dimensional printing. 3Dvol. 5. Print Addit Manuf; 2018. p. 185–93. https://doi.org/10.1089/3dp.2018.0004.

[12] Edelen DL, Bruck HA. Predicting failure modes of 3D-printed multi-material polymer sandwich structures from process parameters. Journal of Sandwich Structures & Materials 2022;24:1049–75. https://doi.org/10.1177/10996362211020445.

[13] Tee YL, Peng C, Pille P, Leary M, Tran P. PolyJet 3D printing of composite materials: experimental and modelling approach. JOM 2020;72:1105–17. https://doi.org/10.1007/s11837-020-04014-w.

[14] Elkaseer A, Chen KJ, Janhsen JC, Refle O, Hagenmeyer V, Scholz SG. Material jetting for advanced applications: a state-of-the-art review, gaps and future directions. Addit Manuf 2022;60:103270. https://doi.org/10.1016/j.addma.2022.103270.

[15] Gülcan O, Günaydın K, Tamer A. The state of the art of material jetting—a critical review. Polymers (Basel) 2021;13:2829. https://doi.org/10.3390/polym13162829.

[16] Tyagi S, Yadav A, Deshmukh S. Review on mechanical characterization of 3D printed parts created using material jetting process. Mater Today Proc 2022;51:1012–6. https://doi.org/10.1016/j.matpr.2021.07.073.

[17] Patpatiya P, Chaudhary K, Shastri A, Sharma S. A review on polyjet 3D printing of polymers and multi-material structures. Proc Inst Mech Eng C J Mech Eng Sci 2022;236:7899–926. https://doi.org/10.1177/09544062221079506.

[18] Shaukat U, Rossegger E, Schlögl S. A review of multi-material 3D printing of functional materials via vat Photopolymerization. Polymers (Basel) 2022;14:2449. https://doi.org/10.3390/polym14122449.

[19] Nazir A, Gokcekaya O, Md Masum Billah K, Ertugrul O, Jiang J, Sun J, et al. Multi-material additive manufacturing: a systematic review of design, properties, applications, challenges, and 3D printing of materials and cellular metamaterials. Mater Des 2023;226:111661. https://doi.org/10.1016/j.matdes.2023.111661.

[20] Pugalendhi A, Ranganathan R, Chandrasekaran M. Effect of process parameters on mechanical properties of VeroBlue material and their optimal selection in PolyJet technology. The International Journal of Advanced Manufacturing Technology 2020;108:1049–59. https://doi.org/10.1007/s00170-019-04782-z.

[21] Doubrovski EL, Tsai EY, Dikovsky D, Geraedts JMP, Herr H, Oxman N. Voxel-based fabrication through material property mapping: a design method for bitmap printing. Computer-Aided Design 2015;60:3–13. https://doi.org/10.1016/j.cad.2014.05.010.

[22] Kaweesa D, Bobbio L, Beese AM, Meisel NA. Prediction and validation of composite mechanical properties resulting from voxel-based microstructural design in material jetting. Rapid Prototyp J 2023;29:488–503. https://doi.org/10.1108/RPJ-12-2021-0343.

[23] Yuan C, Wang F, Rosen DW, Ge Q. Voxel design of additively manufactured digital material with customized thermomechanical properties. Mater Des 2021;197:109205. https://doi.org/10.1016/j.matdes.2020.109205.

[24] Ulu FI, Mohan RV. Voxel and stereolithographic digital design framework in additive manufacturing: effects in a PolyJet printing process and relevant digital solutions. Progress in Additive Manufacturing 2021;6:653–62. https://doi.org/10.1007/s40964-021-00186-2.

[25] Ulu F, Tomar RPS, Mohan R. Processing and mechanical behavior of rigid and flexible material composite systems formed via voxel digital design in polyjet additive manufacturing. Rapid Prototyp J 2021;27:617–26. https://doi.org/10.1108/RPJ-06-2020-0119.

[26] Mora S, Pugno NM, Misseroni D. 3D printed architected lattice structures by material jetting. Mater Today 2022;59:107–32. https://doi.org/10.1016/j.mattod.2022.05.008.

[27] Bezek LB, Chatham CA, Dillard DA, Williams CB. Mechanical properties of tissue-mimicking composites formed by material jetting additive manufacturing. J Mech Behav Biomed Mater 2022;125:104938. https://doi.org/10.1016/j.jmbbm.2021.104938.

[28] Reckert A, Lang V, Weingarten S, Johne R, Klein J-H, Ihlenfeldt S. Quality prediction and classification of process parameterization for multi-material jetting by means of computer vision and machine learning. Journal of Manufacturing and Materials Processing 2024;8:8. https://doi.org/10.3390/jmmp8010008.

[29] Pugalendhi A, Ranganathan R, Ganesan S. Impact of process parameters on mechanical behaviour in multi-material jetting. Mater Today Proc 2021;46:9139–44. https://doi.org/10.1016/j.matpr.2019.12.106.

[30] Aslani K-E, Korlos A, Kechagias JD, Salonitis K. Impact of process parameters on dimensional accuracy of PolyJet 3D printed parts using grey Taguchi method. MATEC Web of Conferences 2020;318:01015. https://doi.org/10.1051/matecconf/202031801015.

[31] Chand R, Sharma VS, Trehan R, Gupta MK, Sarikaya M. Investigating the dimensional accuracy and surface roughness for 3D printed parts using a multi-jet printer. J Mater Eng Perform 2023;32:1145–59. https://doi.org/10.1007/s11665-022-07153-0.

[32] Meisel NA, Dillard DA, Williams CB. Impact of material concentration and distribution on composite parts manufactured via multi-material jetting. Rapid Prototyp J 2018;24:872–9. https://doi.org/10.1108/RPJ-01-2017-0005.

[33] Vu IQ, Bass LB, Williams CB, Dillard DA. Characterizing the effect of print orientation on interface integrity of multi-material jetting additive manufacturing. Addit Manuf 2018;22:447–61. https://doi.org/10.1016/j.addma.2018.05.036.

[34] Bass L, Meisel NA, Williams CB. Exploring variability of orientation and aging effects in material properties of multi-material jetting parts. Rapid Prototyp J 2016;22:826–34. https://doi.org/10.1108/RPJ-11-2015-0169.

[35] Gay P, Blanco D, Pelayo F, Noriega A, Fernández P. Analysis of factors influencing the mechanical properties of flat PolyJet manufactured parts. Procedia Eng 2015;132:70–7. https://doi.org/10.1016/j.proeng.2015.12.481.

[36] Yap YL, Wang C, Sing SL, Dikshit V, Yeong WY, Wei J. Material jetting additive manufacturing: an experimental study using designed metrological benchmarks. Precis Eng 2017;50:275–85. https://doi.org/10.1016/j.precisioneng.2017.05.015.

[37] Tee YL, Tran P, Leary M, Pille P, Brandt M. 3D printing of polymer composites with material jetting: mechanical and fractographic analysis. Addit Manuf 2020;36:101558. https://doi.org/10.1016/j.addma.2020.101558.

[38] Dinzart F, Sabar H. New micromechanical modeling of the elastic behavior of composite materials with ellipsoidal reinforcements and imperfect interfaces. Int J Solids Struct 2017;108:254–62. https://doi.org/10.1016/j.ijsolstr.2016.12.024.

[39] Gu GX, Chen CT, Richmond DJ, Buehler MJ. Bioinspired hierarchical composite design using machine learning: simulation, additive manufacturing, and experiment. Mater Horiz 2018;5:939–45. https://doi.org/10.1039/c8mh00653a.

[40] Yang C, Kim Y, Ryu S, Gu GX. Prediction of composite microstructure stress-strain curves using convolutional neural networks. Mater Des 2020:189. https://doi.org/10.1016/j.matdes.2020.108509.

[41] Goh GD, Yap YL, Agarwala S, Yeong WY. Recent Progress in additive manufacturing of Fiber reinforced polymer composite. Adv. Mater Technol 2019:4. https://doi.org/10.1002/admt.201800271.

[42] Egan PF, Gonella VC, Engensperger M, Ferguson SJ, Shea K. Computationally designed lattices with tuned properties for tissue engineering using 3D printing. PloS One 2017:12. https://doi.org/10.1371/journal.pone.0182902.

[43] Wei X, Bhardwaj A, Shih C-C, Zeng L, Tai B, Pei Z. Experimental investigation of Stratasys J750 PolyJet printer: Effects of orientation and layer thickness on mechanical properties. Volume 1: Additive manufacturing; manufacturing equipment and systems; bio and sustainable manufacturing, American Society of Mechanical Engineers; 2019. doi:https://doi.org/10.1115/MSEC2019-2717.

[44] Yuan C, Wang F, Qi B, Ding Z, Rosen DW, Ge Q. 3D printing of multi-material composites with tunable shape memory behavior. Mater Des 2020;193:108785. https://doi.org/10.1016/j.matdes.2020.108785.

[45] Lumpe TS, Mueller J, Shea K. Tensile properties of multi-material interfaces in 3D printed parts. Mater Des 2019;162:1–9. https://doi.org/10.1016/j.matdes.2018.11.024.

[46] Heo H, Jin Y, Yang D, Wier C, Minard A, Dahotre NB, et al. Manufacturing and characterization of hybrid bulk Voxelated biomaterials printed by digital anatomy 3D printing. Polymers (Basel) 2020;13:123. https://doi.org/10.3390/polym13010123.

[47] Ionita CN, Mokin M, Varble N, Bednarek DR, Xiang J, Snyder K V., et al. Challenges and limitations of patient-specific vascular phantom fabrication using 3D Polyjet

printing. In: Molthen RC, Weaver JB, editors., 2014, p. 90380M. doi:https://doi.org/10.1117/12.2042266.
[48] Ituarte IF, Boddeti N, Hassani V, Dunn ML, Rosen DW. Design and additive manufacture of functionally graded structures based on digital materials. Addit Manuf 2019;30:100839. https://doi.org/10.1016/j.addma.2019.100839.
[49] Slesarenko V, Rudykh S. Towards mechanical characterization of soft digital materials for multimaterial 3D-printing. Int J Eng Sci 2018;123:62–72. https://doi.org/10.1016/j.ijengsci.2017.11.011.
[50] Khalifeh S. OPTIMIZED POLYMERIC STRUCTURES OF ORGANIC ACTIVE ELECTRONIC COMPONENTS. Polymers in Organic Electronics, Elsevier 2020: 251–339. https://doi.org/10.1016/B978-1-927885-67-3.50011-0.
[51] Woehrmann M, Toepper M. Polymerization of thin film polymers. New polymers for special applications. InTech 2012. https://doi.org/10.5772/48205.
[52] Engels T. Thermoset adhesives: epoxy resins, acrylates and polyurethanes. Thermosets, Elsevier 2012:228–53. https://doi.org/10.1533/9780857097637.2.228.
[53] Abdellaoui H, Raji M, Bouhfid R, Qaiss A el kacem. Investigation of the deformation behavior of epoxy-based composite materials. Failure analysis in biocomposites, fibre-reinforced composites and hybrid composites, Elsevier; 2019, p. 29–49. doi:https://doi.org/10.1016/B978-0-08-102293-1.00002-4.
[54] Billah SMR. Dielectric Polymers 2018:1–49. https://doi.org/10.1007/978-3-319-92067-2_8-1.
[55] Wang C, Sun Q, Zhao L, Jia J, Yao L, Peng Z. Mechanical and dielectric strength of laminated epoxy dielectric graded materials. Polymers (Basel) 2020;12:622. https://doi.org/10.3390/polym12030622.
[56] Mueller J, Courty D, Spielhofer M, Spolenak R, Shea K. Mechanical properties of interfaces in inkjet 3D printed single- and multi-material parts. 3Dvol. 4. Print Addit Manuf; 2017. p. 193–9. https://doi.org/10.1089/3dp.2017.0038.
[57] Daneshdoost N. Tensile performance data of 3D printed MMJ composite samples. Mendeley Data 2024. https://doi.org/10.17632/ny3h2739hg.2.
[58] Mueller J, Shea K, Daraio C. Mechanical properties of parts fabricated with inkjet 3D printing through efficient experimental design. Mater Des 2015;86:902–12. https://doi.org/10.1016/j.matdes.2015.07.129.
[59] Peloquin J, Kirillova A, Mathey E, Rudin C, Brinson LC, Gall K. Tensile performance data of 3D printed photopolymer gyroid lattices. Data Brief 2023;49:109396. https://doi.org/10.1016/j.dib.2023.109396.
[60] Grimaldo Ruiz O, Rodriguez Reinoso M, Ingrassia E, Vecchio F, Maniero F, Burgio V, et al. Design and mechanical characterization using digital image correlation of soft tissue-mimicking polymers. Polymers (Basel) 2022;14:2639. https://doi.org/10.3390/polym14132639.
[61] Swallowe GM. Strain rate effects. In: Mechanical properties and testing of polymers. vol. 3. Dordrecht: Springer; 1999. p. 214–8. https://doi.org/10.1007/978-94-015-9231-4_47.
[62] Su FY, Sabet FA, Tang K, Garner S, Pang S, Tolley MT, et al. Scale and size effects on the mechanical properties of bioinspired 3D printed two-phase composites. J Mater Res Technol 2020;9:14944–60. https://doi.org/10.1016/j.jmrt.2020.10.052.
[63] Giri J, Chiwande A, Gupta Y, Mahatme C, Giri P. Effect of process parameters on mechanical properties of 3d printed samples using FDM process. Mater Today Proc 2021;47:5856–61. https://doi.org/10.1016/j.matpr.2021.04.283.
[64] Samykano M, Selvamani SK, Kadirgama K, Ngui WK, Kanagaraj G, Sudhakar K. Mechanical property of FDM printed ABS: influence of printing parameters. The International Journal of Advanced Manufacturing Technology 2019;102:2779–96. https://doi.org/10.1007/s00170-019-03313-0.
[65] Frunzaverde D, Cojocaru V, Bacescu N, Ciubotariu C-R, Miclosina C-O, Turiac RR, et al. The influence of the layer height and the filament color on the dimensional accuracy and the tensile strength of FDM-printed PLA specimens. Polymers (Basel) 2023;15:2377. https://doi.org/10.3390/polym15102377.
[66] Somireddy M, Singh CV, Czekanski A. Analysis of the material behavior of 3D printed laminates via FFF. Exp Mech 2019;59:871–81. https://doi.org/10.1007/s11340-019-00511-5.
[67] Nambu S, Michiuchi M, Inoue J, Koseki T. Effect of interfacial bonding strength on tensile ductility of multilayered steel composites. Compos Sci Technol 2009;69:1936–41. https://doi.org/10.1016/j.compscitech.2009.04.013.
[68] Liew KM, Pan ZZ, Zhang LW. An overview of layerwise theories for composite laminates and structures: development, numerical implementation and application. Compos Struct 2019;216:240–59. https://doi.org/10.1016/j.compstruct.2019.02.074.
[69] Lorriot Th, Marion G, Harry R, Wargnier H. Onset of free-edge delamination in composite laminates under tensile loading. Compos B Eng 2003;34:459–71. https://doi.org/10.1016/S1359-8368(03)00016-7.
[70] Huang T, Bobyr M. A review of delamination damage of composite materials. Journal of Composites Science 2023;7:468. https://doi.org/10.3390/jcs7110468.
[71] Phillipps AJ, Clegg WJ, Clyne TW. The failure of layered ceramics in bending and tension. Composites 1994;25:524–33. https://doi.org/10.1016/0010-4361(94)90180-5.
[72] Meshi I, Amarilio I, Benes D, Haj-Ali R. Delamination behavior of UHMWPE soft layered composites. Compos B Eng 2016;98:166–75. https://doi.org/10.1016/j.compositesb.2016.05.027.
[73] Qadeer A, Hussain G, Alkahtani M, Buhl J. Springback behavior of a metal/polymer laminate in incremental sheet forming: stress/strain relaxation perspective. J Mater Res Technol 2023;23:1725–37. https://doi.org/10.1016/j.jmrt.2023.01.088.
[74] Christke S, Gibson AG, Grigoriou K, Mouritz AP. Multi-layer polymer metal laminates for the fire protection of lightweight structures. Mater Des 2016;97:349–56. https://doi.org/10.1016/j.matdes.2016.02.105.
[75] Fu S-Y, Feng X-Q, Lauke B, Mai Y-W. Effects of particle size, particle/matrix interface adhesion and particle loading on mechanical properties of particulate–polymer composites. Compos B Eng 2008;39:933–61. https://doi.org/10.1016/j.compositesb.2008.01.002.
[76] Nanoth R, Jayanarayanan K, Sarath Kumar P, Balachandran M, Pegoretti A. Static and dynamic mechanical properties of hybrid polymer composites: a comprehensive review of experimental, micromechanical and simulation approaches. Compos Part A Appl Sci Manuf 2023;174:107741. https://doi.org/10.1016/j.compositesa.2023.107741.
[77] Guo G, Alam S, Peel LD. An investigation of deformation and failure mechanisms of fiber-reinforced composites in layered composite armor. Compos Struct 2022;281:115125. https://doi.org/10.1016/j.compstruct.2021.115125.
[78] Zhang Y, Qiao J, Zhang G, Li Y, Li L. Prediction of deformation and failure behavior of continuous fiber reinforced composite fabricated by additive manufacturing. Compos Struct 2021;265:113738. https://doi.org/10.1016/j.compstruct.2021.113738.
[79] Monti M, Palenzona M, Fiorino F, Baudach F, Onnis A, Romeo A. Design, manufacturing and FEA prediction of the mechanical behavior of a hybrid-molded polycarbonate / continuous carbon fiber reinforced composite component. Compos B Eng 2022:238. https://doi.org/10.1016/j.compositesb.2022.109891.
[80] Ning F, Cong W, Qiu J, Wei J, Wang S. Additive manufacturing of carbon fiber reinforced thermoplastic composites using fused deposition modeling. Compos B Eng 2015;80:369–78. https://doi.org/10.1016/j.compositesb.2015.06.013.
[81] Sun J, Yu S, Wade-Zhu J, Chen X, Binner J, Bai J. 3D printing of layered ceramic/carbon fiber composite with improved toughness. Addit Manuf 2022;50:102543. https://doi.org/10.1016/j.addma.2021.102543.
[82] Kumar R, Chohan JS, Kumar R, Yadav A, Piyush Kumar P. Metal spray layered hybrid additive manufacturing of PLA composite structures: mechanical, thermal and morphological properties. J Thermoplast Compos Mater 2022;35:1387–407. https://doi.org/10.1177/0892705720932622.
[83] Liu Q, Xu R, Zhou Y, Ge J, Yuan S, Long Y, et al. Metamaterials mapped lightweight structures by principal stress lines and topology optimization: methodology, additive manufacturing, ductile failure and tests. Mater Des 2021:212. https://doi.org/10.1016/j.matdes.2021.110192.
[84] Bashir U, Hassan A, Ahmed F, Zain-ul-abdein M, Mobeen H, Dildar A, et al. Thermo-mechanical analysis of additive manufacturing for material properties estimation of layered polymer composite. Mechanics of Advanced Materials and Structures 2023:1–11. https://doi.org/10.1080/15376494.2023.2255258.
[85] Dimas LS, Bratzel GH, Eylon I, Buehler MJ. Tough composites inspired by mineralized natural materials: computation, 3D printing, and testing. Adv Funct Mater 2013;23:4629–38. https://doi.org/10.1002/adfm.201300215.
[86] Gao S, Liu R, Xin H, Liang H, Wang Y, Jia J. The surface characteristics, microstructure and mechanical properties of peek printed by fused deposition modeling with different raster angles. Polymers (Basel) 2022:14. https://doi.org/10.3390/polym14010077.
[87] Liu F, Li T, Jiang X, Jia Z, Xu Z, Wang L. The effect of material mixing on interfacial stiffness and strength of multi-material additive manufacturing. Addit Manuf 2020;36:101502. https://doi.org/10.1016/j.addma.2020.101502.
[88] Karama M, Afaq KS, Mistou S. Mechanical behaviour of laminated composite beam by the new multi-layered laminated composite structures model with transverse shear stress continuity. Int J Solids Struct 2003;40:1525–46. https://doi.org/10.1016/S0020-7683(02)00647-9.
[89] Noor AK, Kim YH, Peters JM. Transverse shear stresses and their sensitivity coefficients in multilayered composite panels. AIAA Journal 1994;32:1259–69. https://doi.org/10.2514/3.12128.